Imaging Neural Activity Using MEG and EEG

Tremendous progress has been made over the last decade in the development of techniques for producing macroscopic images of brain activity. Positron emission tomography (PET) can produce high-resolution images of activated areas using radionucleides designed to image regional cerebral blood flow [1]. Functional magnetic resonance imaging (fMRI) also uses changes in cerebral blood flow to produce images of neural activation[2]. While PET and fMRI are capable of producing images with spatial resolution on the order of a few millimeters, their temporal resolution is fundamentally limited by the time constants of the hemodynamic effects that result from neural activation and which are exploited to produce these activation images.

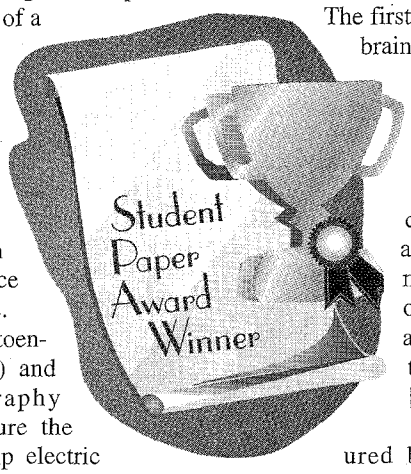

In contrast, magnetoencephalography (MEG) and electroencephalography (EEG) directly measure the magnetic field or scalp electric potentials caused by neural activation and have temporal resolutions on the order of a few milliseconds. Thus, MEG and EEG provide unique insights into the dynamic aspects of brain activity. Due to the ambiguity of the associated quasistatic inverse problem, however, high spatial resolution images of neural activity from EEG and MEG data can not be produced using linear inverse methods of the kind used in processing fMRI and PET data.

In this article we describe an alternative approach to the inverse problem in which a Bayesian framework is used to incorporate anatomical constraints on the location of the activation sites, with a probabilistic model for the spatio-temporal distribution of activity over these regions. We describe EEG and MEG instrumentation, review the forward model, and discuss weighted minimum norm techniques. We also provide a simulation example showing the Bayesian method applied to the problem of imaging dynamic sources confined to a realistic human brain surface.

Overview of MEG and EEG

MEG is a relatively new modality in which measurements are made of the magnetic field produced by current sources in the brain. These extremely small magnetic fields can be measured using a SQUID (superconducting quantum interference device) magnetometer. The first measurements of the brain's magnetic field using this device were made by Cohen in 1972 [3]. However, only within the past few years have clinical systems been available that allow simultaneous collection of the magnetic field at a large number of locations around the head [4-5].

The EEG, first measured by Hans Berger in 1929, has been used in the study of brain function and disease for several decades. Again, only fairly recently have high-quality digital acquisition systems been developed to provide the many channels of data over the entire head that are required to solve the inverse problem [6]. In the early days, MEG was believed to be inherently superior to EEG for the purposes of localizing brain activity, due to the decreased dependence of the MEG forward model on accurate knowledge of the conductivity properties of the head. Currently however, EEG and MEG are more commonly viewed as complementary modalities and are often collected simultaneously[7-8].

The major sources of both the EEG and MEG are widely accepted to be localized current sources in the cerebral cortex. Much of the literature uses a set of equivalent current dipoles to represent these localized sources and solves the inverse problem by finding the location and moments of these dipoles using nonlinear numerical optimization methods. Attempts at estimating equivalent current sources based on EEG measurements date back to Shaw in 1955 [9], whereas the earliest source localization from MEG data was reported by Brenner in 1978 [10]. Extensions of the dipole fitting method to consider the temporal components of the data were developed by Scherg and Von Cramon [11], and methods that reduced the dimensionality of the search space using signal subspace methods were developed by Mosher, et al. [12].

The major limitation of fitting a few current dipoles to the data is that the resulting fits may not well represent more distributed cortical sources. Constraining solutions to the cortex is also difficult when using multiple dipole models. To overcome these limitations, a number of researchers have addressed the MEG/EEG inverse problem as one of image reconstruction. Most imaging methods that have been studied to date are based on weighted minimum norm techniques [13]. The imaging problem is highly ill-posed due both to the inherent non-uniqueness of the quasistatic inverse problem and to the limited number of sensor measurements available. The Bayesian method we present in this article attempts to overcome the ill-posedness of the inverse problem by introducing a probabilistic model for the source image. This model is based on the observation that activation in the cortex tends to be sparse and focal.

Instrumentation

The signals generated by EEG and MEG are very weak, with MEG exceptionally so. EEG data are typically measured in microvolts (μv), as the potential difference

James W. Phillips[1], Richard M. Leahy[1], John C. Mosher[2], and Bijan Timsari[1]
[1]Signal & Image Processing Institute
University of Southern California
[2]Los Alamos National Laboratory Biophysics Group

 0739-5175/97/$10.00©1997

between two points on the scalp. MEG signals are typically measured in femtoTeslas (fT), a magnetic field about nine orders of magnitude weaker than the Earth's magnetic field. Acquisition of these magnetic fields generally requires magnetic shielding of the subject and superconducting magnetic sensors in special configurations. We briefly review here the sensor systems used for EEG and MEG.

The first and most critical clinical element in EEG recording is the electrode, which is usually attached to the scalp with a conductive gel intermediary. Ideally, the impedance of all electrode-scalp interfaces is identical and as low as possible, but this is difficult to achieve due to varying electrode composition and a changing interface resulting from electrode movement. A large number of electrodes are generally placed about the scalp at known locations, with one acting as a reference electrode. Hence, each "channel" in an EEG system represents the potential difference between two electrodes, with most of the channels sharing a common reference electrode.

The EEG signal must be amplified, nominally 10,000 times, before digital acquisition and recording. At the front end is a high gain pre-amplifier with a high input impedance so as not to draw current from the scalp and distort the measurements. The pre-amplifier output is then further conditioned and amplified to meet the specific requirements of the analog-to-digital converter. The user selects the bandwidths of interest, typically a sub-kilohertz range of frequencies, and the system sets the necessary filters and sampling rates for digital acquisition.

The "noise" in an EEG system is generally dominated by biological signals, i.e., well-designed EEG systems are generally insensitive to environmental contamination. Strong radio stations and power-line frequencies can couple into the EEG leads, but careful system design and properly attached electrodes mitigate these effects. In contrast, the extremely sensitive MEG sensors must operate in environmental noise conditions many orders of magnitude stronger than the biological signals of interest. The key components to successful neuromagnetic recordings include careful magnetic shielding of the sensors and special differential sensor configurations. The technology that makes recordings of these fT fields possible is the SQUID.

A SQUID is a superconducting device comprising one or more Josephson junctions. For our purposes, we may think of the SQUID magnetometer as a device for converting the magnetic flux passing through a coil into a voltage that varies sinusoidally with increasing flux. SQUID electronics modulate this sinusoidal output to lock into a single period of the sine function (a flux "quantum") and thereby linearize the flux-to-voltage relationship. In MEG, the SQUID is typically operated in a feedback loop that effectively nulls the flux passing through pickup coil. The electronics monitor the amount of feedback energy required to null the flux, yielding a "null detector" sensor system of extreme sensitivity. Wikswo [5] presents a review of the SQUID development and its use in biomagnetism.

The SQUID magnetometer has a single pickup coil of nominally one to two cm diameter. The extreme sensitivity of this device restricts its use to magnetically shielded rooms. As an alternative or addition to magnetic shielding, SQUID *gradiometers* have two or more pickup coils arranged to effectively form differential inputs. The Earth's static magnetic field is canceled in these gradiometers, allowing the possibility of operating them in unshielded environments. However, even these devices remain sensitive to variations of the local field, usually caused by the movements of nearby vehicles and other, large ferromagnetic objects. Thus, clinical settings will typically still require magnetically shielded rooms. These rooms can cost hundreds of thousands of dollars, motivating the continual development of novel sensor designs to reduce the level of required shielding; see Wikswo [5] for a more detailed review of some of these more recent designs.

Cryogenic dewars contain the liquid helium used to achieve superconductivity and usually contain both pickup coils and SQUIDs. The cost and complexity of such systems led to the initial development of SQUID systems containing only a few channels. These sensors, such as the BTi seven-channel system, were suspended from a mechanical gantry that allowed the dewar to be moved about a subject's head, but any one placement had limited spatial coverage. More recently, large arrays comprising hundreds of magnetometers or gradiometers have been developed. Figure 1 is a diagram of a SQUID array inside a multi-channel MEG gradiometer system.

The need for cryogenics, however, has restricted the design of whole-head multi-channel systems to rigid helmet shapes, which by necessity must be de-

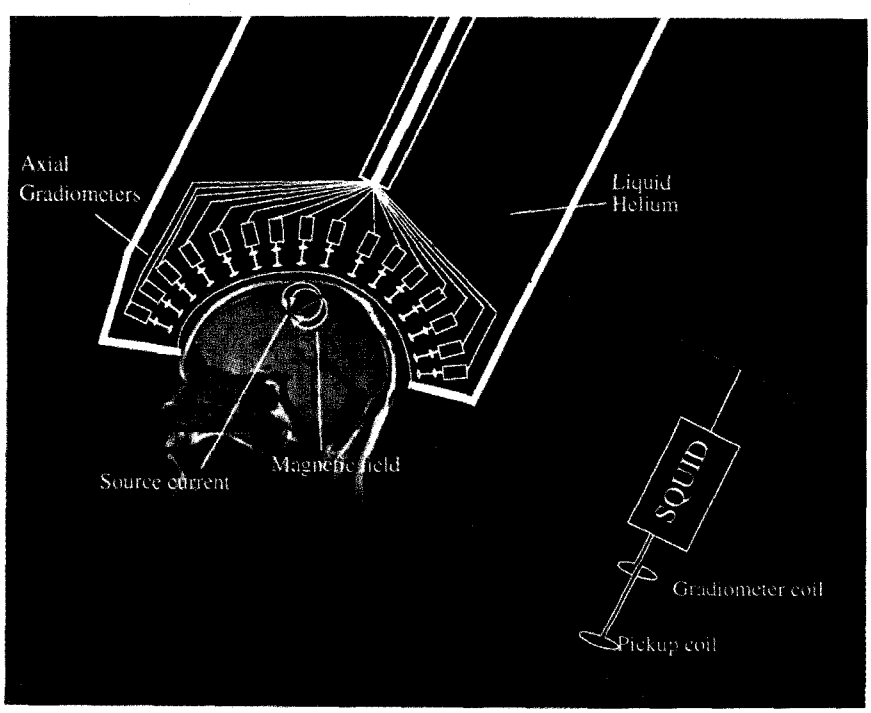

1. Schematic representation of an axial gradiometer system with whole-head coverage. The pickup and gradiometer coils are oppositely wound, such that the Earth's static magnetic field is canceled. The weak neural current is effectively detected only by the nearby pickup coil.

signed to accommodate the largest head expected. The coils are thus effectively further away from the scalp of subjects with smaller heads, reducing some of the sensor sensitivity. Nonetheless, several whole-head MEG systems have been recently introduced that allow the simultaneous acquisition of neural signals over the entire head (cf. [4-5]).

Regardless of the methods used to control environmental noise, both EEG and MEG are heavily influenced by what may be called "brain noise." In brain mapping, a researcher may be interested, for instance, in the cortical response to a specific auditory, visual, or somatosensory stimulus. In the milliseconds following such a stimulus, however, these "event-related" responses are dominated by much stronger on-going neural activity. Many experimental paradigms, such as auditory tones, can be easily repeated, and averaging the data generally suppresses the on-going activity to reveal the event-related responses. Averaging 100 or more trials is typical in order to adequately reveal these weak responses.

Neural Sources and the Forward Model

The major sources of both EEG and MEG are believed to be current flow along the apical dendrites of the pyramidal cells in the cerebral cortex [14]. These dendrites are arranged in a columnar fashion to be locally normal to the cortical surface. This columnar arrangement results in a coherent summation of the current fields for near-synchronous activation of a large number of neurons within a small area of cortex. This focal activity can be represented by an equivalent current dipole located approximately at the center of this area, with its moment normal to the cortical surface. Thus, a single focal source in the cortex can be modeled using a single equivalent current dipole. More complex distributions can be modeled using several current dipoles. In the imaging approach to the MEG/EEG inverse problem, sources are constrained to a tessellated representation of the cerebral cortex, with a current dipole located at the centroid of each surface element. We now briefly describe the relationship between these current sources and the observed signals.

For the biological signals of interest in EEG and MEG, the time-derivatives of the associated electric and magnetic fields are sufficiently small that the fields may be considered quasistatic. We represent this neural activity as a current density, $\boldsymbol{j}(\boldsymbol{r})$, in a closed volume of finite conductivity. Outside this volume, the conductivity and current density are zero. The integral equation relating the magnetic field $\boldsymbol{b}(\boldsymbol{r})$ and the current density $\boldsymbol{j}(\boldsymbol{r})$ is the well known integral form of the Biot-Savart law:

$$\boldsymbol{b}(\boldsymbol{r}) = \frac{\mu_0}{4\pi}\int_G \boldsymbol{j}(\boldsymbol{r}')\times \boldsymbol{d}\,/\,d^3 d\boldsymbol{r}' \tag{1}$$

where $\boldsymbol{d} = \boldsymbol{r}-\boldsymbol{r}'$ is the distance between the observation point, $\boldsymbol{r}$, and the source point, $\boldsymbol{r}'$. The integration is carried out over a closed volume, G. The constant μ_0 is the permittivity of free space, which is the generally applied assumption for biological tissues.

We divide the current into two components, *passive* and *primary*. We define as passive those currents that are a result of the macroscopic electric field in the conducting medium of the volume, $\boldsymbol{j}^v(\boldsymbol{r}) = \sigma(\boldsymbol{r})\boldsymbol{E}(\boldsymbol{r})$. All other currents are considered primary, $\boldsymbol{j}^p(\boldsymbol{r})$. The division of the current as $\boldsymbol{j}^p(\boldsymbol{r})$ and $\boldsymbol{j}^v(\boldsymbol{r})$ is to emphasize that neural activity gives rise to macroscopic primary currents that then flow passively throughout the rest of the conducting medium. The *forward problem* is to determine the potentials and magnetic fields that result from these primary currents. The *inverse problem* is to locate these primary currents and hence the sources of brain activity. Under the assumption described above that the EEG and MEG are primarily due to dendritic currents in the pyramidal cells, we would expect the solution to the inverse problem to have the primary current confined to the cerebral cortex.

Substituting our interpretation of $\boldsymbol{j}(\boldsymbol{r})$ into Eq. (1) yields:

$$\boldsymbol{b}(\boldsymbol{r}) = \frac{\mu_0}{4\pi}\int_G (\boldsymbol{j}^p(\boldsymbol{r}') - \sigma(\boldsymbol{r}')\nabla v(\boldsymbol{r}'))\times \boldsymbol{d}\,/\,d^3 d\boldsymbol{r}' \tag{2}$$

where, because of the quasistatic assumptions, the electric field can be modeled as the gradient of a scalar potential, $\boldsymbol{E}(\boldsymbol{r}) = -\nabla v(\boldsymbol{r})$. The typical head model assumes the conductivity, $\sigma(\boldsymbol{r})$, is piece-wise constant and isotropic. The gradient of the conductivity is therefore zero, except at the surfaces between regions, which allows the volume integrals to be reworked into surface integrals. We assume our volume can be divided into $M + 1$ regions

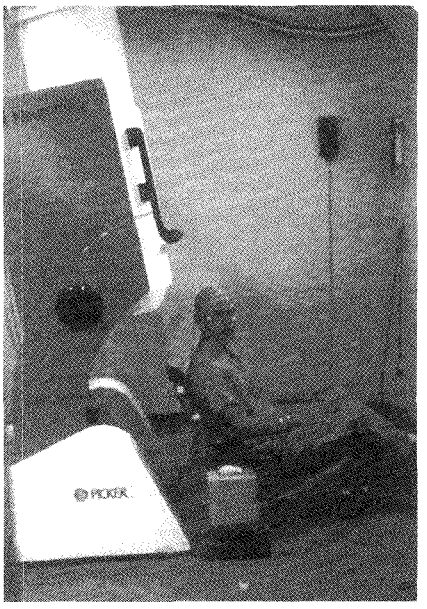

2. A subject wearing a whole-head 64-channel EEG electrode cap next to the Neuromag-122 MEG planar gradiometer system [4] in preparation for a combined EEG/MEG study.

with conductivities σ_i, $i = 1,\ldots,M+1$, which includes the nonconducting region outside of the head. These regions are separated from adjacent regions by a total of $m \geq M$ surfaces, S_i. Through simple vector identities, we can rewrite the volume integral in Eq. (2) as [15]:

$$\boldsymbol{b}(\boldsymbol{r}) = \boldsymbol{b}_\infty(\boldsymbol{r}) - \frac{\mu_0}{4\pi}\sum_{i=1}^{m}(\sigma_i^- - \sigma_i^+)\left(\int_{S_i} v(\boldsymbol{r}')\boldsymbol{n}_i(\boldsymbol{r}')\times \boldsymbol{d}\,/\,d^3\right)d\boldsymbol{d} \tag{3}$$

where $\boldsymbol{n}_i(\boldsymbol{r})$ is the "outward" directed unit vector normal to the ith surface, and the "+" ("–") superscript indicates the conductivity outside (inside) the ith surface. The *primary field*, $\boldsymbol{b}_\infty(\boldsymbol{r})$, is:

$$\boldsymbol{b}_\infty(\boldsymbol{r}) = \frac{\mu_0}{4\pi}\int_G \boldsymbol{j}^p(\boldsymbol{r}')\times \boldsymbol{d}\,/\,d^3 d\boldsymbol{r}' \tag{4}$$

which is the magnetic field observed at $\boldsymbol{r}$ due to the primary current only. If no boundaries were present, then $\boldsymbol{b}_\infty(\boldsymbol{r})$ would represent the magnetic field generated by a primary source in an infinite homogeneous medium.

To compute the magnetic field using Eq. (3), we must first know the potential $v(\boldsymbol{r})$ on all boundaries. Using Green's theorem, we can obtain a surface integral equation for $v(\boldsymbol{r})$ for $\boldsymbol{r}$ on the jth surface (see [16] for details):

$$v_\infty(\boldsymbol{r}) = \frac{(\sigma_j^- + \sigma_j^+)}{2} v(\boldsymbol{r}) + \frac{1}{4\pi} \sum_{i=1}^{m} (\sigma_i^- - \sigma_i^+) \int_{S_i} v(\boldsymbol{r}') \boldsymbol{n}_i(\boldsymbol{r}') \cdot \boldsymbol{d} / d^3 d\sigma' \quad \boldsymbol{r} \in S_j \tag{5}$$

where we have assumed all surfaces are smooth, and $v_\infty(\mathbf{r})$ is the primary potential, i.e., the solution for the infinite homogeneous medium due to the primary current $\boldsymbol{j}^p(\boldsymbol{r})$:

$$v_\infty(\boldsymbol{r}) = \frac{1}{4\pi} \int_G \boldsymbol{j}^p(\boldsymbol{r}') \cdot \boldsymbol{d} / d^3 d\boldsymbol{r}' \tag{6}$$

Equation (3) and Eq. (5) therefore form our general set of equations for solving the forward problem for scalp potentials (EEG) and external magnetic fields (MEG). The primary currents enter the equations as volume integrals in Eq. (4) and Eq. (6). If we assume that the primary current exists only at a discrete point, i.e., the primary current source is a current dipole $\boldsymbol{q}$ located at $\boldsymbol{r}_q$, then $\boldsymbol{b}_\infty(\boldsymbol{r})$ and $v_\infty(\boldsymbol{r})$ can be simplified as:

$$\boldsymbol{b}_\infty(\boldsymbol{r}) = (\mu_0 / 4\pi) \boldsymbol{q} \times (\boldsymbol{r} - \boldsymbol{r}_q) / d^3 \tag{7}$$

$$v_\infty(\boldsymbol{r}) = (1 / 4\pi) \boldsymbol{q} \cdot (\boldsymbol{r} - \boldsymbol{r}_q) / d^3 \tag{8}$$

By superposition, any solution we find for the point dipole can be used in a summation over an arbitrary number of dipoles. We will therefore focus our presentation on the solution of the forward problem for a single dipole with moment $\boldsymbol{q}$ located at $\mathbf{r}_q$.

It is generally impossible to find an analytic solution for the magnetic field and surface potentials for arbitrarily shaped conductive regions. In general, the potentials must first be solved numerically using Eq. (5) and Eq. (6), solving the EEG forward problem. The potentials are then used with Eq. (3) and Eq. (4) to solve the MEG forward problem. If, however, we assume that the head is a spherically symmetric conductor, we can then find closed-form solutions for these current dipole sources [15-17]. The use of this model in EEG and MEG applications has been prevalent in the biomagnetism community, due to the simplicity of the forward model equations. Figure 3 shows how this spherically symmetric model can be applied to the human head.

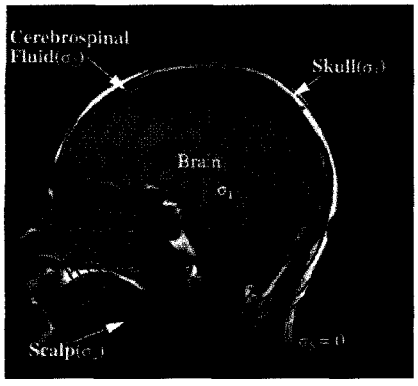

3. The human head modeled as a set of concentric spheres, each with uniform isotropic conductivity, σ_i.

The MEG sensors are often oriented normal to the local scalp curvature, and can thereby be assumed to be sensitive only to the radial component of the magnetic field. In this case, the MEG solution for the spherical model becomes quite simple, i.e., the radial component of Eq. (7) [17].

This formula may be extended to account for the nonradial magnetic field as well. A key modeling advantage of the spherical assumption is that the magnetic field can be computed without knowing the conductivity profile, σ. One consequence of the spherical assumption is that if a dipole is radially oriented (has no tangential components), then the magnetic field measured outside the head will be zero. The MEG measurement, in this case, is sensitive only to the two tangential components of any dipole moment. (See Sarvas [17] for a more complete development of the solution for the spherical model).

The forward model calculation for EEG using a spherical head model is more complex than that of MEG. The conductivities must be specified, and thus the model must include specific assumptions about the sphere radii. Although a single sphere model has a closed form representation, the analytic solution of the multisphere model has an infinite summation representation. (See Cuffin and Cohen [7] for a presentation in a four-sphere case).

Although we have discussed simple solutions for a spherically symmetric head, the forward model can be calculated for arbitrary head geometries using boundary element methods. The review by Hämäläinen, et al. [4], provides an overview of the groundwork and related references for setting up the system of equations to be solved. The explicit determination of the vertices required to define the scalp, skull, and brain surfaces must be extracted from anatomical MR or CT images. The computational requirements for generating and solving these boundary element problems have in the past been difficult to justify in clinical situations. The recent move toward the integration of whole-head sensor systems with other functional and anatomical modalities, as well as dramatic increases in CPU speeds, should result in a trend toward the use of more complex and realistic head models in routine analyses.

Regardless of which assumptions are used to compute the forward model for MEG or EEG, the data generated by the jth single dipole with moment $\boldsymbol{q}_j$ may always be expressed as the inner product of a vector kernel and the dipole moment, $b_i = \mathbf{k}_{ij} \cdot \boldsymbol{q}_j$, where b_i is the ith sensor measurement, and $\mathbf{k}_{ij}$ is the final forward model result relating the jth current dipole with the ith sensor. In the work that follows, we will assume that the possible locations of the dipoles have been restricted to the cortex, and that at each cortical location the orientation of the dipole has been restricted to lie in the direction normal to the local cortical surface. If we denote this known orientation as $\hat{\boldsymbol{q}}_j$ and the corresponding unknown amplitude as y_j, then our data model may be represented as:

$$b_i = (\boldsymbol{k}_{ij} \cdot \hat{\boldsymbol{q}}_j) y_j = g_{ij} y_j \tag{9}$$

where g_{ij} is the "gain" of the constrained source at position j to the magnetic field (MEG) or potential (EEG) at sensor i. When we consider a set of N dipoles and M sensors (both EEG and MEG) over L time samples, the equation becomes $\mathbf{B} = \mathbf{GY}$, where $\mathbf{B}$ is the $M \times L$ spatio-temporal data matrix, $\mathbf{G}$ is the $M \times \mathrm{N}$ "gain matrix" found from the appropriate EEG and MEG forward model calculations, and $\mathbf{Y}$ is the $N \times L$ matrix of unknown cortical source amplitudes.

The Inverse Problem

The inverse problem is to find the neural current source distribution given a series of magnetic field and/or scalp potential measurements. The solution is ambiguous, since an infinite number of current fields within the brain can produce identical scalp potential and external magnetic field distributions. The problem is exacerbated by the limited number of sensor measurements available. To find a physiologically meaningful solution, we can constrain the primary sources to the cerebral cortex by tessellating the brain surface extracted from an MR scan of the subject. A point dipole, with orientation normal to the surface, as described above, can then be used to approximate the current distribution over each of the surface patches. Thus, the MEG/EEG imaging problem can be reduced to that of finding

the primary current sources distributed over the cortical surface.

Using the linear model described above, we can modify the forward problem to account for noise:

$$\mathbf{B} = \mathbf{GY} + \mathbf{N} \tag{10}$$

where **G** is a kernel matrix determined from the forward model. The $M \times L$ matrix **N** represents noise inherent in the system, as was discussed in the section on instrumentation. Below, we use $\mathbf{y}(t)$ to denote the dipole amplitudes at time t, i.e., the t'th column of **Y**.

In order to adequately represent sulci in the image, the number of triangles used in our tessellation must be very large, generally far more than the number of sensors (N»M). The inverse problem is therefore highly under-determined. Minimum norm methods [13-17] overcome this problem by finding a solution that matches the data at time sample t while minimizing a weighted l_2-norm of the solution vector:

$$\mathbf{y}_{\text{wmn}}(t) = \min_{\mathbf{y}} \mathbf{y}^{\mathrm{T}}\mathbf{C}_{\mathbf{y}}^{-1}\mathbf{y}$$
$$\text{subject to } \|\mathbf{b}(t) - \mathbf{Gy}\|^2 = 0 \tag{11}$$

which results in the closed-form solution:

$$\mathbf{y}_{\text{wmn}}(t) = \mathbf{C}_{\mathbf{y}}\mathbf{G}^{\mathrm{T}}(\mathbf{G}\mathbf{C}_{\mathbf{y}}\mathbf{G}^{\mathrm{T}})^{-1}\mathbf{b}(t) \tag{12}$$

where $\mathbf{C}_{\mathbf{y}}$ is a positive definite weighting matrix. These weighted minimum norm approaches can result in very blurred reconstructions, which tend to be superficial, and the problem can be unstable due to poor conditioning of the system matrix. The superficiality can be compensated for, to some extent, by selecting different weighting matrices. The problem may be stabilized through Tikhonov regularization [18], but the solutions remain blurred [19]. These minimum norm methods also do not take into account temporal information, treating each time sample individually. In the following section, we adopt a Bayesian approach to imaging, which introduces temporal correlation into the solutions while avoiding the blurring exhibited by the minimum methods.

Bayesian Imaging

We may reformulate the problem by treating the source image, **Y**, as a random field. We may then represent the prior knowledge we have regarding the nature of neural sources in the form of a prior probability, $p(\mathbf{Y})$. We combine this with a probabilistic description of the data $p(\mathbf{B}|\mathbf{Y})$, conditioned on the image **Y**, and use Bayes theorem to find the posterior distribution:

$$p(\mathbf{Y}|\mathbf{B}) = \frac{p(\mathbf{B}|\mathbf{Y})p(\mathbf{Y})}{p(\mathbf{B})} \tag{13}$$

The image **Y** that maximizes this posterior probability, called the maximum *a posteriori* (MAP) estimate, can be used as our estimate of the neural sources.

Studies using fMRI and PET reveal the highly sparse and localized nature of activation in the cerebral cortex. We wish to develop a prior density on **Y** that reflects this behavior. In a prior publication [19], we developed this posterior density for a single time slice, and we present it here for a time series of data. To better represent the sparse focal nature of neural activity into our prior, we use a binary indicator process, **x**, to model whether each source dipole is on ($x_i = 1$) or off ($x_i = 0$). Those sites that are active are assumed to have a temporally white Gaussian amplitude, $z_i(t)$, where t is the time sample ($\mathbf{t} = 1...L$). We can write the ($N \times$L) source image matrix **Y** as:

$$\mathbf{Y} = \mathbf{XZ} \tag{14}$$

where $\mathbf{X} = \text{diag}(\mathbf{x})$ is a diagonal matrix. Assuming independence of the indicator and amplitude processes, we can write the posterior probability for **x** and **Z**, given the MEG data matrix **B** as:

$$p(\mathbf{x},\mathbf{Z}|\mathbf{B}) = \frac{p(\mathbf{B}|\mathbf{x},\mathbf{Z})p(\mathbf{x})p(\mathbf{Z})}{p(\mathbf{B})} \tag{15}$$

The joint probability $p(\mathbf{x})$ is chosen to reflect the expectation that sources are sparse and focal. To achieve this goal, we use a Markov random field (MRF) model, for which sparse focal sources have a higher probability of occurring than more distributed sources. We define the prior to be a Gibbs distribution, $p(\mathbf{x}) = \frac{1}{z}\exp\{-V(\mathbf{x})\}$, with energy function:

$$V(\mathbf{x}) = L\sum_{\mathbf{i}}\left[\underbrace{\alpha_i x_i}_{\substack{\text{Sparseness}\\ \text{Term}}} + \underbrace{\beta_i\left[\sum_{j\in\xi_i}(x_i - x_j)^2\right]^{Q}}_{\text{Clustering Term}}\right] \tag{16}$$

where L is the number of time samples, and $\alpha_i > 0$ and $\beta_i > 0$ determine the relative weights of the sparseness and clustering terms, Q determines the severity of the clustering, and the neighborhood ξ_i is defined as the pixel's nine nearest neighbors. Note that if $Q \neq 1$, the terms raised to the Qth power become coupled, and the neighborhood effectively dilates pixel i's neighborhood to include the 30 nearest neighbors. Figure 4 shows the pixel neighborhood.

The α_i and β_i terms allow us to incorporate into our density knowledge we may have from other functional imaging modalities, such as fMRI or PET. This allows us to change the clustering properties or favor sources in certain areas of the cortex. For our purposes here, however, we assume no specific prior information regarding source locations, and set $\alpha_i = \alpha$ and $\beta_i = \beta$ for all $i = 1...N$. Three images obtained by sampling from $p(\mathbf{x})$ for various values of α and β are shown in Fig. 5.

We assume that if a pixel is on, then its amplitude is temporally independent Gaussian with spatial covariance matrix $\mathbf{C}_{\mathbf{z}}$:

$$p(\mathbf{Z}) = \frac{1}{K_z}\exp\left\{-\frac{1}{2}\text{Tr}\left\{\mathbf{Z}^{\mathrm{T}}\mathbf{C}_z^{-1}\mathbf{Z}\right\}\right\} \tag{17}$$

where K_z is a normalization constant and Tr{ } is the trace of the matrix. We assume that the noise is also temporally independ-

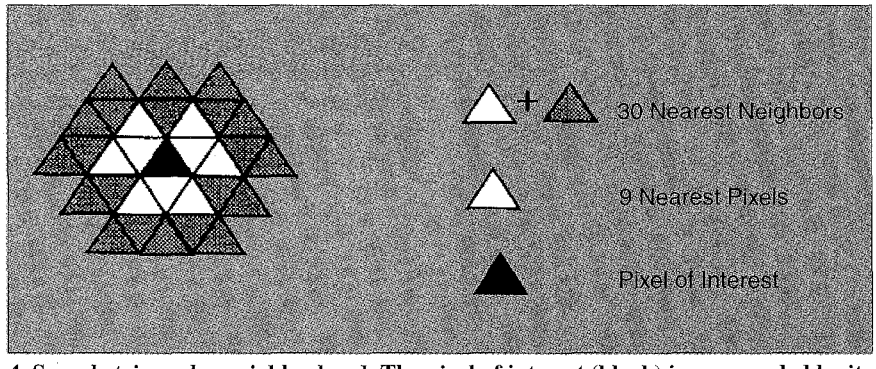

4. Sample triangular neighborhood. The pixel of interest (black) is surrounded by its 9 nearest pixels (white). The overall neighborhood is a dilation of these 9 nearest pixels, comprised of the 30 nearest neighbors (white and shaded).

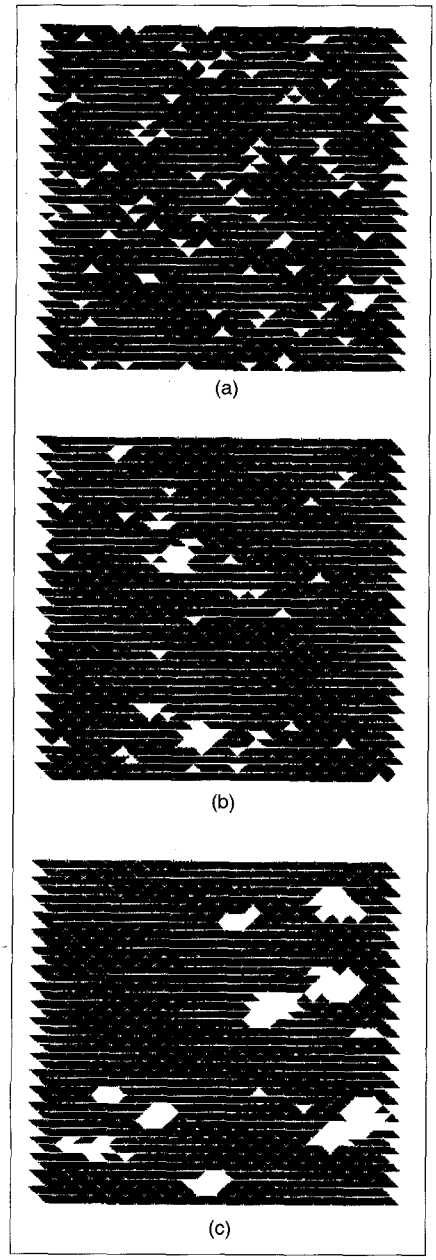

5. Three images obtained by sampling from $p(\mathbf{x})$. White triangles signify an *on* pixel. For each, $\alpha = 0.20$. (a) $\beta = 0.17, Q = 1$ (b) $\beta = 0.05, Q = 2$ (c) $\beta = 0.012, Q = 3$.

ent Gaussian with spatial covariance matrix $\mathbf{C_n}$. We may express the likelihood function as:

$$p(\mathbf{B}|\mathbf{x},\mathbf{Z}) = \frac{1}{K_n}\exp\left\{-\frac{1}{2}\mathrm{Tr}\left\{[\mathbf{B}-\mathbf{GXZ}]^{\mathrm{T}}\mathbf{C}_{\mathbf{n}}^{-1}[\mathbf{B}-\mathbf{GXZ}]\right\}\right\} \tag{18}$$

The posterior density is defined by the likelihood function given in Eq. (18) and the priors on $\mathbf{x}$ and on $\mathbf{Z}$ given in Eq. (16) and Eq. (17). The posterior density is a Gibbs distribution with posterior energy function:

$$U(\mathrm{x},\mathrm{Z}|\mathrm{B}) = \frac{1}{2}\mathrm{Tr}\left\{[\mathbf{B}-\mathbf{GXZ}]^{\mathrm{T}}\mathbf{C}_{\mathbf{n}}^{-1}[\mathbf{B}-\mathbf{GXZ}]+\mathbf{Z}^{\mathrm{T}}\mathbf{C}_{\mathbf{z}}^{-1}\mathbf{Z}\right\} + V(\mathbf{x}) \tag{19}$$

This posterior gives a complete probabilistic description of $\mathbf{x}$ and $\mathbf{Z}$, from which we can, in principle, compute moments such as the posterior mean and variance. In this article we consider only computation of the posterior mode or MAP (maximum *a posteriori*) solution.

The MAP Solution Using Mean Field Annealing

We have described a mean field annealing approach (MFA) for maximizing this posterior density in a prior publication [19], and present a brief summary here. Minimizing an energy function of discrete and continuous variables is a difficult task. Since the function is quadratic in $\mathbf{Z}$, however, we can derive a closed-form expression for the optimal $\mathbf{Z}^*(\mathbf{x})$ given any particular indicator process. Setting the derivative of Eq. (19), with respect to $\mathbf{Z}$, to zero and solving yields:

$$\mathbf{Z}^*(\mathbf{x}) = \mathbf{C_z}\mathbf{X}\mathbf{G}^{\mathrm{T}}(\mathbf{GXC_z}\mathbf{XG}^{\mathrm{T}}+\mathbf{C_n})^{-1}\mathbf{B} \tag{20}$$

Substituting $\mathbf{Z}^*(\mathbf{x})$ into $U(\mathbf{x},\mathbf{Z}|\mathbf{B})$ results in:

$$\tilde{U}(\mathbf{x}|\mathbf{B}) = \mathbf{U}(\mathbf{x},\mathbf{Z}|\mathbf{B})|_{\mathbf{Z}=\mathbf{Z}^*(\mathbf{x})} \tag{21}$$

which is a Gibbs energy function for the density $\tilde{p}(\mathbf{x}|\mathbf{B})$, a function of $\mathbf{x}$ only. We have now transformed the problem to a minimization of a function of a binary random process only. Numerous methods exist to find the minimum of this type of function. We choose a method based on MFA, which forms a temperature-dependent posterior density and approximates the mean field of this density at ever decreasing temperatures, until the algorithm converges to a local minimum as $T \rightarrow 0$.

Coordinate-wise descent using iterated conditional modes (ICMs) moves quickly to a poor local minimum. MFA [20], on the other hand, uses a computation of the mean, and forces this mean to become binary as we lower a temperature parameter, T, to zero. This allows us to move within the $\{0,1\}^N$ hypercube to arrive perhaps at a better local minimum. We effectively create a new temperature dependent posterior density:

$$p_T(\mathbf{x}|\mathbf{B}) = \frac{1}{K_T}\exp\{-U(\mathbf{x}|\mathbf{B})/T\} \tag{22}$$

If the mean field can be found at any temperature, T, then this mean will approach the energy function minimum as $T \rightarrow 0$, i.e., the MAP solution [19].

We compute the mean field using mean field approximation [21] with the following update strategy:

$$x_i^{(n+1)} = E_T\{x_i|x_j^{(n)} \quad \forall j \neq i\} \tag{23}$$

where n is the iteration number. In this, we cycle through all the pixels in the image, finding the expected value of each pixel given that all other pixels in the image are equal to their mean values. Since we do not know these other mean values, we begin with an arbitrary initialization and cycle through the image many times, until the algorithm converges to an approximation of the true mean field.

Simulations

We have conducted simulations based on a 3-D source model. We used the array configuration of the Neuromag-122 system (Neuromed Ltd., Helsinki, Finland [4]) for MEG and simulated 133 EEG sensors equally spaced about the upper hemisphere of a spherically symmetric head at a radius of 9.5 cm. An image of the brain surface beneath the representation of the Neuromag sensors and the associated EEG sensors is shown in Fig. 6.

To form the reconstruction region we first extracted the brain surface from the MR image of a subject using morphological techniques [22]. We then used an implicit surface polygonizer to tessellate the surface [23]. To adequately represent

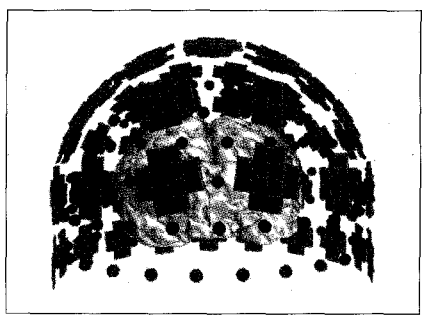

6. Computer rendering of the brain surface extracted from an MR image shown under the 61 Neuromag-122 dual-planar gradiometers (green squares) and the 133 EEG sensor locations (black spheres).

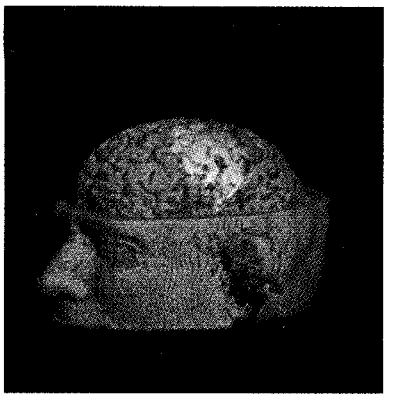

7. Volume rendering of the brain used in the simulations. The brain is shown with only the upper half of the skull removed. The brain is shown in bronze, the patch is white in color, and all areas of activity are shown in red. Three clusters of activity are located inside the white patch.

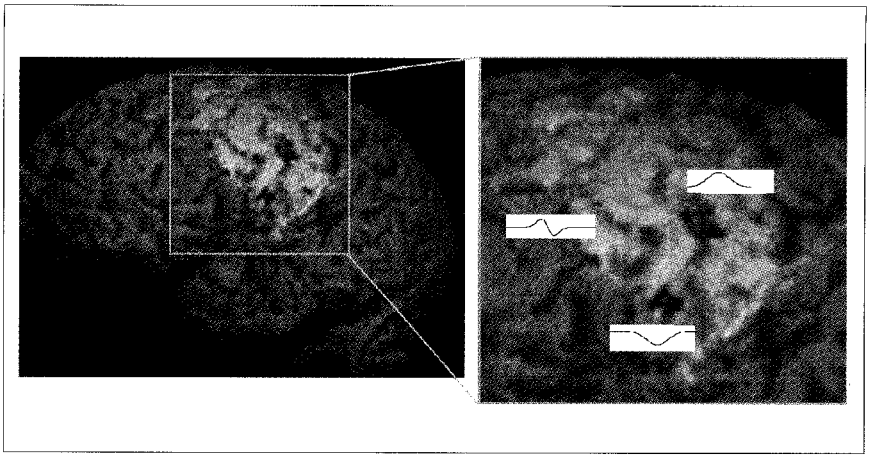

8. A sample source image used in the MEG/EEG simulations. Three clusters are present, shown in red. The 10-point time-series for each cluster is plotted next to each cluster.

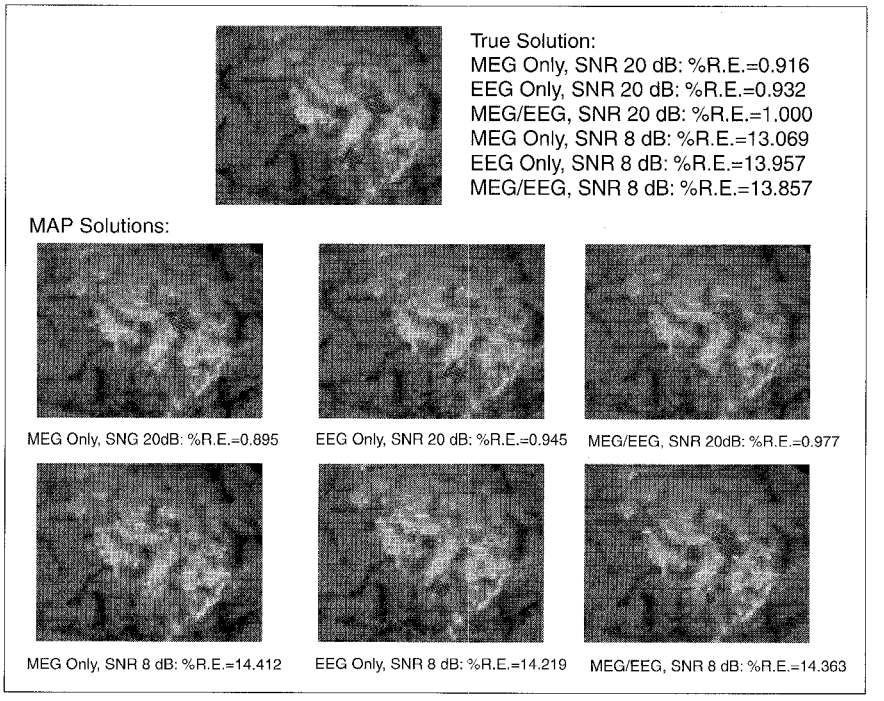

9. Sample 3-D simulation, white Gaussian noise added: 122 MEG gradiometer measurements, 133 EEG measurements, and 2,000 point reconstruction region.

sulci in the image, we had to use a very fine tessellation density. Tessellation of the entire brain using this algorithm, therefore, resulted in a surface composed of over 23,000 triangles. To make the problem more manageable, we extracted a patch composed of a subset of 2,000 of these triangles for our simulations. Figure 7 shows a volume rendering of the brain surface and the patch we extracted from it. We constrained all sources to be normal to the local cortical surface.

The two characteristics of primary significance in choosing the parameters of the prior $p(\mathbf{x})$ for our simulation are the average number of active regions (clusters) and their average size. By qualitative inspection of images on our reconstruction region sampled from this prior, we determined that $Q = 2.5$ gives acceptable control over the average number of clusters and cluster size by adjusting only the parameters α and β. We then used Markov chain Monte Carlo methods [24] to compute the average number of clusters and cluster size as a function of the parameters α and β. We assumed 2-3 clusters on average, with an area of 0.3 cm^2 for each cluster. We found that appropriate parameter values for the surface patch used in our simulation were $\alpha = 0.210$ and $\beta = 0.070$. We assumed Z was temporally and spatially white Gaussian noise with variance σ_i^2=100 nAm $i = 1...N$. This value was chosen to reflect typical activity seen in an evoked response study. We set $\mathbf{C_n}$ to $\nu \cdot \mathbf{I}$, where ν is the added noise variance that we assume known.

For the simulation, we chose a time series for $\mathbf{Z}$ assuming that all sources have the same time series across a cluster and that they are formed by the "Hermite-type" wave functions of Geva, et al. [25]. An image of a random sampling on $\mathbf{x}$ with a 10-point time-series using the Hermite waveforms is shown in Fig. 8.

The results of a representative simulation are shown in Fig. 9. White Gaussian noise was added to the data to achieve a desired SNR, defined as the average signal power at each sensor divided by the noise variance at the sensor. The percent residual error (%R.E.) shown is defined as:

$$100\left[\frac{\mathrm{Tr}\{(\mathbf{GY}-\mathbf{B})^{\mathrm{T}}(\mathbf{GY}-\mathbf{B})\}}{\mathrm{Tr}\{\mathbf{B}^{\mathrm{T}}\mathbf{B}\}}\right]\% \tag{24}$$

We have found that combining MEG and EEG results in a superior performance when compared to using the modalities individually. Note that this is a simulation, and all noise was considered white Gaussian. In reality, noise variances for MEG and EEG may be very different, so combining the two modalities should be performed with caution in regard to noise issues and the formation of $\mathbf{C_n}$.

In the 8dB case, all solutions clearly misplaced one or more of the clusters.

This shows that at lower SNRs, it is impossible to resolve between the true configuration and the Bayesian reconstruction, since both exhibit the sparse clustered property of our prior.

Conclusions

We have developed a Bayesian framework for image estimation from combined MEG/EEG data. Our results indicate that performance of our imaging approach is superior to that of weighted minimum norm when the image is sparse and focal. Note however that if the image is not sparse, our method would perform poorly since our prior is specifically designed to give sparse focal sources. This observation serves to emphasize the fact that the use of prior information is crucial in extracting useful spatial information from the data.

We have also found that combining MEG and EEG gives superior results when compared to using the modalities individually. This improvement is due not only to increasing the number of measurements, but also because of the complimentary nature of MEG/EEG [7, 8]. Even when working with the two modalities in combination, significant limitations to electromagnetic imaging exist. Regardless of the number and placement of sensors, reconstructions are generally only reliable if relatively few source clusters exist. If a large number of distributed sources exist, no imaging technique can hope to reconstruct them accurately strictly from the MEG/EEG data given. Such complex distributions will generally be matched as well or better by simpler solutions. Thus, if used on their own, we expect MEG/EEG data to be most useful when the number of activated sites is small. Alternatively, when used in combination with fMRI or PET, it may be possible to produce dynamic images of more complex processes.

Acknowledgments

This work was supported by the National Institute of Mental Health Grant No. RO1-MH53213, and by Los Alamos Laboratory, operated by the University of California for the United States Department of Energy under contract W-7405-ENG-36.

James Phillips was born in Murray, Kentucky, in 1965. He received his B.S.E.E. in electrical engineering from Vanderbilt University in 1988 and served four years in the United States Marine Corps as a tank platoon commander. After an honorable discharge in 1992, he went on to earn his M.S.E.E. from the University of Kentucky in 1994 and has just completed his Ph.D. from the University of Southern California. His research interests lie in the area of signal and image processing and stochastic optimization related to linear inverse problems.

Richard Leahy was born in Surrey, England, in 1960. He received the B.Sc. and Ph.D. degrees in electrical engineering from the University of Newcastle upon Tyne, England, in 1981 and 1985 respectively. In 1985 he joined the University of Southern California where he is currently an Associate Professor and Director of the Signal and Image Processing Institute of the Department of Electrical Engineering -Systems. He also holds joint appointments with the Departments of Radiology and Biomedical Engineering at USC. His research interests lie primarily in the application of signal and image processing theory to biomedical inverse problems. His current research involves the reconstruction and analysis of medical images with an emphasis on PET, MEG, and MRI.

John C. Mosher received his Bachelors in Electrical Engineering with highest honors from the Georgia Institute of Technology in 1983. From 1979-1983 he was also a cooperative education student with Hughes Aircraft Company in Fullerton, California. From 1983-1993, he worked at TRW in Fullerton, California, researching signal analysis procedures for electromagnetic pulse effects. While at TRW, he received his M.S. and Ph.D. in electrical engineering from the Signal & Image Processing Institute of the University of Southern California in 1985 and 1993, respectively. Upon graduation, he accepted a staff position at the Los Alamos National Laboratory, Los Alamos, New Mexico (USA),where he researches the forward and inverse modeling problems of electrophysiological recordings. A member of the Biophysics Group, his interests also include the general source localization and imaging problems, both in neuroscience work and in other novel applications of sensor detection.

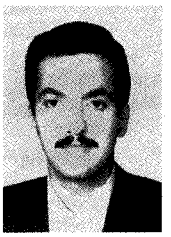

Bijan Timsari was born in Iran, on September 11, 1967. He received the BSc degree from Sharif University of Technology in 1990 and the M.S. degree from Isfehan University of Technology in 1993, both in Electrical Engineering. Since 1994 he has been working in the Signal and Image Processing Institute at the University of Southern California where he received his MSEE degree in 1996. He is now working toward his Ph.D. degree. His research interests include image processing, computer vision, and computer graphics.

Address for Correspondence: Richard M. Leahy, Signal and Image Processing Institute, University of Southern California, 3740 McClintock Avenue, Los Angeles, CA 90089-2564.

References

1. **Grafton ST, Woods RP, Mazziotta JC, Phelps ME:** Somatotopic mapping of the primary motor cortex in humans: activation studies with cerebral blood flow and positron emission tomography. *J of Neurophysiol* 47 (3): 735-743, 1991.
2. **Frahm J, Merboldt K-D, Hanicke W:** Functional MRI of human brain activation at high spatial resolution. *Magnetic Resonance in Medicine* 29 (1): 139-144, 1993.
3. **Cohen D:** Magnetoencephalography: detection of the brain's electrical activity with a superconducting magnetometer. *Science* 175: 664-666, 1972.
4. **Hamalainen MS, Hari R, Ilmoniemi RJ, Knuutila J, Lounasmaa OV:** Magnetoencephalography -theory, instrumentation, and applications to noninvasive studies of the working human brain. *Rev of Mod Phys* 65 (2): 413-497, 1993.
5. **Wikswo JP:** SQUID magnetometers for biomagnetism and nondestructive testing: important questions and initial answers. *IEEE Trans on Applied Superconductivity* 5 (2): 74-120, 1995.
6. **Gevins A, Le J, Martin NK, Brickett P, Desmond J, Reutter B:** High resolution EEG - 124-channel recording, spatial deblurring and MRI integration methods. *Electroenceph Clin Neurophysiol* 90: 337-358, 1994.
7. **Cuffin BN, Cohen D:** Comparison of the magnetoencephalogram and electroencephalogram," *Electroenceph Clin Neurophysiol* 47: 132-146, 1979.
8. **Mosher JC, Spencer ME, Leahy RM, Lewis PS:** Error bounds for EEG and MEG dipole source localization. *Electroenceph Clin Neurophysiol* 86: 303-321, 1993.
9. **Shaw JC, Roth M:** Potential distribution analysis, I. A new technique for the analysis of

electrophysiological phenomena. *Electroenceph Clin Neurophysiol* 7: 273-284, 1955.
10. **Brenner D, Williamson SJ, Kaufman L:** Visually evoked magnetic fields of the human brain. *Science* 190: 480-482, 1975.
11. **Scherg M, von Cramon D:** Two bilateral sources of the late AEP as identified by a spatio-temporal dipole model. *Electroenceph Clin Neurophysiol* 62: 32-44, 1985.
12. **Mosher JC, Lewis PS, Leahy RM:** Multiple dipole modeling and localization from spatio-temporal MEG data. *IEEE Trans Biomed Eng* 39: 541-557, 1992.
13. **Wang JZ, Williamson SJ, Kaufman L:** Magnetic source images determined by a lead-field analysis: the unique minimum-norm least-squares estimation. *IEEE Trans Biomed Eng* 39 (7): 665-675, 1992.
14. **Okada Y:** Neurogenesis of evoked magnetic fields. in: Williamson SJ, Romani GL, Kaufman L, Midena I:*Biomagnetism, an Interdisciplinary Approach*, Plenum Press, NY, 399-408, 1983.
15. **Geselowitz D:** On bioelectric potentials in an inhomogeneous volume conductor. *Biophysics J* (7): 1-11, 1967.
16. **Barr RC, Pilkington TC, Boineau PC, Spach MS:** Determining surface potentials from current dipoles, with application to electrocardiography. *IEEE Trans Biomed Eng* 13 (2): 88-92, April 1966.
17. **Sarvas J:** Basic mathematical and electromagnetic concepts of the biomagnetic inverse problem. *Phys in Med Biol* 32: 11-22, 1987.
18. **Hansen PC:** *Regularization Tools, A Matlab Package for Analysis and Solution of Discrete Ill-Posed Problems*, available in Postscript from http://www.mathworks.com/, March 1993.
19. **Phillips JW, Leahy RM, Mosher JC:** MEG-Based Imaging of Focal Neuronal Current Sources. *IEEE Trans Med Imag*, in press.
20. **Bilbro G, Mann R, Miller TK, Snyder WE Van den Bout DE, et al:** Optimization by mean field annealing. in: Touretzky DS, *Advances in Neural Information Processing Systems*, Morgan-Kauffman, San Mateo, CA: 91-98, 1989.
21. **Chandler D:** *Introduction to Modern Statistical Mechanics*, Oxford University Press, 131-138, 1987.
22. **Sandor S, Leahy R:** Surface-based labeling of cortical anatomy using a deformable atlas. *IEEE Trans Med* Imag 16 (1): 41-54, 1997.
23. **Bloomenthal J:** Polygonization of implicit surfaces. *Computer Aided Geometric Design* 5 (4): 53-60, 1988.
24. **Goutsias J:** Markov random fields: interacting particle systems for statistical image modeling and analysis. *Johns Hopkins University Technical Report JHU/ECE 90-01*, 1996.
25. **Geva AB, Pratt H, Zeevi YY:** Spatio-temporal multiple source localization by wavelet-type decomposition of evoked potentials. *Electroenceph Clin Neurophysiol* 96: 278-286, 1995.

News Notes

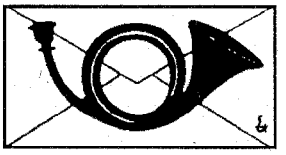

Drug Pump on a Chip

Driven partly by managed healthcare's desire to keep people out of hospitals and by the needs of diabetics and other patients on regular intravenous medication, biomedical engineers have built a prototype drug pump the size of a contact lens—a miniature closed-loop implant that could monitor its own flow rate to ensure a steady stream of medicine.

The pump is still considered large as far as microelectromechanical systems are concerned, in which sensors, actuators, and electronics are merged onto a single silicon wafer. The next step will be to shrink the device so it can be mass produced like a computer chip. It is hoped that this device may be adapted as a closed-loop system for monitoring blood glucose levels and pumping just the right amount of insulin into the blood stream.

The prototype consists of a rectangular silicon chamber with one of the outer walls made of two thin layers a titanium-nickel alloy sandwiched around a layer of silicon. The alloy forcefully changes shape when heated to around 60 degrees Celsius (140 F).

To operate the pump, rhythmic pulses of mild electrical current are passed directly through the alloy, setting up a cycle of heating and cooling that causes the metal to flex. This forces the chamber to expand and contract. The expansion pulls the fluid into the chamber through an intake valve, and the contraction expels the fluid through an exhaust valve.

The flow sensor is made up of a heater that raises the temperature of the fluid at one point in the flow stream. Two heat sensors downstream detect this hot spot as it passes by. From this measurement the flow rate can be calculated. The device has been bench-tested successfully and is being scaled down for mass production.

About 20 million miniature blood pressure sensors are now being used each year, but there are still are no closed-loop systems on the market that can regulate themselves without a doctor's intervention.

Bioengineer Selected for Entrepreneur-in-Residence Program at WPI

Robert J. Harvey will be Worcester Polytechnic Institute's Entrepreneur-In-Residence during the 1997 fall term. During his residence this successful bioengineer will present public seminars on new directions in biomedical engineering, offer a course that will feature case studies of his start-up enterprises, and serve as distinguished professor in biomedical engineering.

Harvey co-founded Thoratec Laboratories Corp., Berkeley, Calif., in 1976 with J. Donald Hill, M.D., chief of cardiovascular surgery at California Pacific Medical Center in San Francisco. Harvey recently retired as chair, CEO, and president of the company, which is a pioneer in circulatory support for failing hearts, arterial grafts for repairing diseased blood vessels, and the licensing of blood contacting biomaterials.

Harvey earned his undergraduate degree at the United States Military Academy, West Point; his master's in physics at Drexel University, Philadelphia; and his doctorate in biomedical engineering at WPI. For several years preceding his doctorate he was employed at the Thermo Electron Corp., long identified with its entrepreneurial founder, George Hatsopoulos, where Harvey played a role in diversifying the company in the biomedical field with the first fully integrated artificial heart.

Following his doctorate and before establishing Thoratec, Harvey founded Mirlin Corp., in Hudson, Mass., in order to pursue the commercial potential of a unique protein sweetener for diabetics. Harvey has served as chair of WPI's biomedical advisory committee since its establishment in 1986.

WPI's Entrepreneurs Collaborative was created in 1993 and has developed an introductory course, a minor, the Entrepreneur-in-Residence program, and many projects involving WPI undergraduates with entrepreneurs in their respective business settings.